Article:

Thiruthummal, A.A., Shelyag, S., Fedun, V. et al. (2026) An information geometry-based method to study atmospheric and seismic phenomena with VLF signals. Earth and Space Science, 13 (7). e2025EA004610. ISSN: 2333-5084

https://doi.org/10.1029/2025ea004610

AGU ADVANCING EARTH AND SPACE SCIENCES

Earth and Space Science

RESEARCH ARTICLE
10.1029/2025EA004610

Key Points:

- A method is proposed to use anomalies in VLF/LF signals to study atmospheric, geophysical, and space weather phenomena
- The method finds anomalies in global VLF/LF signals using an information geometry framework
- The method links signal anomalies to geomagnetic storms and hurricanes

Correspondence to:

A. A. Thiruthummal,
thiruthuma@uni.coventry.ac.uk

Citation:

Thiruthummal, A. A., Shelyag, S., Fedun, V., Ruzheinikov, S., & Kim, E.-j. (2026). An information geometry-based method to study atmospheric and seismic phenomena with VLF signals. *Earth and Space Science*, *13*, e2025EA004610. https://doi.org/10.1029/2025EA004610

Received 24 JUL 2025
Accepted 10 JUN 2026

Author Contributions:
Conceptualization: Abhiram Anand Thiruthummal
Data curation: Abhiram Anand Thiruthummal, Viktor Fedun, Sergey Ruzheinikov
Formal analysis: Abhiram Anand Thiruthummal
Investigation: Abhiram Anand Thiruthummal, Sergiy Shelyag
Methodology: Abhiram Anand Thiruthummal
Project administration: Sergiy Shelyag
Resources: Abhiram Anand Thiruthummal
Software: Abhiram Anand Thiruthummal, Sergey Ruzheinikov
Supervision: Sergiy Shelyag, Eun-jin Kim
Validation: Abhiram Anand Thiruthummal, Sergiy Shelyag, Viktor Fedun, Eun-jin Kim
Visualization: Abhiram Anand Thiruthummal
Writing – original draft: Abhiram Anand Thiruthummal

An Information Geometry-Based Method to Study Atmospheric and Seismic Phenomena With VLF Signals

Abhiram Anand Thiruthummal[1,2], Sergiy Shelyag[3], Viktor Fedun[4], Sergey Ruzheinikov[4], and Eun-jin Kim[1]

[1]Centre for Fluid and Complex Systems, Coventry University, Coventry, UK, [2]School of Information Technology, Deakin University, Geelong, VIC, Australia, [3]College of Science and Engineering, Flinders University, Adelaide, SA, Australia, [4]Plasma Dynamics Group, School of Electrical and Electronic Engineering, The University of Sheffield, Sheffield, UK

Abstract We propose to employ the framework of information geometry to detect anomalies in Very Low Frequency (VLF) and Low Frequency (LF) signal propagation, measured globally across amplitude and phase channels. Using a sliding-window approach, the probability distributions of signal data are compared over adjacent intervals, defining a statistical measure of distinguishability, named information velocity. Information velocity enables the identification of anomalies in VLF/LF signals and connect them to various atmospheric, geophysical, and space weather phenomena. We have shown the effectiveness of information geometry in quantifying signal variability, offering a powerful framework for anomaly detection in VLF data and wider in the geophysical and atmospheric sciences context. The results demonstrate its potential for uncovering insights into ionospheric behavior, atmospheric disturbances, and their interplay with Earth's electromagnetic environment.

1. Introduction

The Very Low Frequency (VLF, 3–30 kHz) and Low Frequency (LF, 30–300 kHz) radio signals have been used to study a variety of ionospheric, geophysical and solar phenomena (Clilverd et al., 2001; Eftaxias et al., 2003; Hayakawa et al., 1996; Hayakawa, 1996; Inan et al., 2010; A. Kumar & Kumar, 2018; McRae & Thomson, 2004; Molchanov & Hayakawa, 1998; Molchanov et al., 1998; Rozhnoi et al., 2009; Raulin et al., 2010; Rozhnoi et al., 2015; Thomson & Clilverd, 2000).

The theoretical foundation for these applications lies in the concept of electromagnetic waveguides. The surface of the Earth and its ionosphere together form a natural waveguide that confines and directs the propagation of VLF/LF waves, as illustrated in Figure 1. This waveguide is sensitive to changes in its boundary conditions, which can be caused by various natural or anthropogenic phenomena. For example, solar radiation increases the levels of ionization in the ionosphere, thus raising its effective height and altering its reflective properties (Williams & Sátori, 2007). Similarly, meteorological processes such as storms and cyclones can modify the refractive index and absorption characteristics of the waveguide, affecting VLF/LF signal propagation (Rozhnoi et al., 2014). Geophysical phenomena such as earthquakes are also known to produce anomalies in VLF/LF signals (Sorokin & Pokhotelov, 2014). During pre-seismic periods, changes in Earth's lithosphere-ionosphere coupling are believed to produce measurable disturbances in VLF/LF signal characteristics, such as amplitude and phase anomalies. These disturbances may provide critical insights into the processes leading up to seismic events, as discussed in models exploring the interaction of seismic activity with electromagnetic wave propagation (Hayakawa et al., 2010; Molchanov et al., 1998, 2006; Molchanov & Hayakawa, 1998; Rozhnoi et al., 2009).

The study of VLF signals has traditionally utilized a combination of empirical and computational approaches to explore their properties and behaviors. Initial investigations often applied Fourier analysis to decompose VLF signals into their spectral components, revealing patterns in the signal (Chang & Helliwell, 1980; Jones, 1973). Another prominent technique involves wavelet transforms, which have proven effective in capturing transient changes in signal amplitude and phase, enabling the identification of brief anomalies linked to phenomena like solar flares, seismic activity, and atmospheric disturbances (Chernogor, 2010; Güzel et al., 2011; Maurya et al., 2014; Righetti et al., 2012). Furthermore, statistical tools such as cross-correlation analysis and Principal Component Analysis (PCA) have been employed to uncover relationships between VLF signal variations and external geophysical or atmospheric events (Bezděková et al., 2022; Hayakawa et al., 2004). Together, these

Writing – review & editing: Abhiram Anand Thiruthummal, Sergiy Shelyag, Viktor Fedun, Eun-jin Kim

techniques have paved the way for more sophisticated machine learning approaches in recent years (Gross & Cohen, 2020; Nardi et al., 2022; Wang et al., 2020)

Information geometry provides a model-free approach using geometric interpretations of probability distributions, enabling the detection and correlation of anomalies across multiple channels. These anomaly correlations are critical for identifying large-scale geophysical phenomena, such as geomagnetic storms and extreme weather events. For instance, anomalies associated with the 2015-03-18 geomagnetic storm and Hurricane Matthew in 2016 exhibit strong correlations, linked to the geometric configuration of Fresnel sensitivity zones and atmospheric dynamics.

This study builds on the existing body of research using a model-free, information-theoretic approach to analyze the VLF signal data. Specifically, we apply the concept of information velocity (Γ) to detect anomalies in signal propagation that may correspond to geophysical, atmospheric or space weather events. Using the data obtained from a global network of VLF/LF transmitters and receivers, we aim to identify patterns and correlations in signal anomalies, enhancing our understanding of their potential as predictive tools. This approach seeks to uncover novel relationships in the complex interactions between the Earth's surface, its atmosphere, and the ionosphere, offering a fresh perspective on the predictive capabilities of VLF signals.

In this study, we used data from a VLF/LF receiver located in Sheffield, UK, with transmitters distributed over the globe. The SHF radio station is built as the UltraMSK software-defined radio system, which employs GPS 1-s pulses as its phase reference. It can simultaneously record the amplitude and phase of MSK (minimum shift keying) modulated signals in the 10–50 kHz frequency range from multiple transmitters. MSK signals have fixed frequencies within a narrow band of 50–100 Hz around the main frequency and exhibit adequate phase stability. The detailed information on the hardware, antenna and software is available on the UltraMSK webpage (UltraMSK, 2026). The frequency and location of each of them are given in Table 1. The geographical distribution is shown in Figure 2. The collected data covers a range from 2013 to 10–11 to 2016-10-27.

The remainder of the paper is organized as follows. Section 2 outlines the methodology used in this work with Section 2.1 providing a brief introduction to the framework of information geometry, Section 2.2 describing how it can be used for detecting anomalies. Section 2.3 proposes how correlation can be used to reduce noise and false positives among the detected anomalies. Section 3 presents the observations and results derived from this analysis. Finally, Section 4 summarizes the findings and explores potential avenues for extending this work.

2. Background and Methodology

2.1. Information Geometry

Information geometry is the study of probability and statistics using the techniques of differential geometry. To achieve this we must first equip the space of all probability distributions with a manifold structure by defining a distance metric between probability distributions. Several different metrics can be defined on a probability space (Diosi et al., 1996; Gangbo & McCann, 1996; Gibbs & Su, 2002; Majtey et al., 2005). In this work we use a metric based on Fisher information (Frieden, 2004) called the Fisher information metric. For a continuous family of probability density functions (PDFs) $p(x;\{\theta\})$ parametrized by a set of continuous parameters $\{\theta\}$, the Fisher information metric $g_{jk}(\{\theta\})$ can be defined as

$$g_{jk}(\theta) := \int_X \frac{\partial \log p(x;\{\theta\})}{\partial \theta_j} \frac{\partial \log p(x;\{\theta\})}{\partial \theta_k} p(x;\{\theta\}) dx, \tag{1}$$

where X denotes the domain of the PDF. In many physically relevant situations including this work, we come across time-dependent PDFs $p(x,t)$ which can be considered as PDFs parameterized by the parameter t. In such cases the Fisher information metric simplifies to

$$g(t) = \int d\mathbf{x} \frac{1}{p(\mathbf{x},t)} \left[\frac{\partial p(\mathbf{x},t)}{\partial t}\right]^2. \tag{2}$$

Using this metric we can now define information length $\mathcal{L}$ as the total distance traveled on the manifold as the PDF evolves with time:

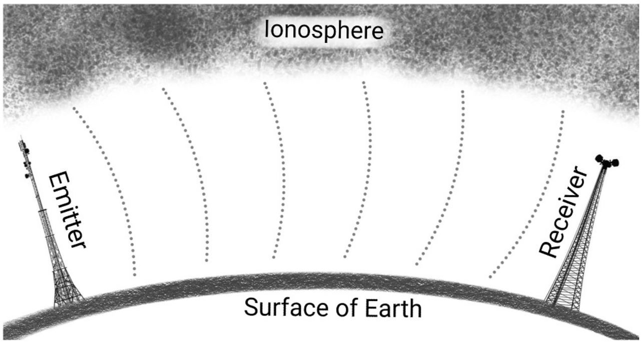

Figure 1. Propagation of VLF/LF signal inside the waveguide made of the surface of Earth and its ionosphere.

$$\mathcal{L}(t) := \int_0^t dt_1 \sqrt{\int d\mathbf{x} \frac{1}{p(\mathbf{x}, t_1)} \left[\frac{\partial p(\mathbf{x}, t_1)}{\partial t_1}\right]^2}. \tag{3}$$

Information length defined in this way is a dimensionless quantity, which quantifies the number of statistically distinguishable states a system has passed through during its temporal evolution (Wootters, 1981).

Using the information length, we can now define an information velocity $\Gamma := \lim_{dt\to 0} d\mathcal{L}/dt$ on the manifold:

$$\Gamma(t) := \sqrt{\int d\mathbf{x} \frac{1}{p(\mathbf{x}, t)} \left[\frac{\partial p(\mathbf{x}, t)}{\partial t}\right]^2}. \tag{4}$$

Γ measures the rate of change of statistically distinguishable states of a time-evolving PDF. Γ has been used to study correlations (Kim, 2021) and abrupt changes in dynamical systems (Guel-Cortez & Kim, 2021). In the context of non-equilibrium thermodynamics, Γ is related to the entropy production rate for a Gaussian process (Kim, 2021) and can be extended to study causality (Kim & Guel-Cortez, 2021).

Note that Equation 4 is numerically unstable when $p \to 0$ due to the presence of $p(\mathbf{x}, t)$ in the denominator. To avoid numerical instability, we can define $q(\mathbf{x}, t) := \sqrt{p(\mathbf{x}, t)}$ and rewrite Γ as follows:

$$\Gamma(t) := 2\sqrt{\int d\mathbf{x} \left[\frac{\partial q(\mathbf{x}, t)}{\partial t}\right]^2}. \tag{5}$$

2.2. Anomaly Detection

Each VLF/LF signal measured by the receiver is characterized by its amplitude and phase. The signals are measured continuously with a sampling interval of 20 s. Since the data is obtained from 17 different transmitters,

Table 1
Location and Frequency of Transmitters and Receivers

Name	Frequency	Latitude	Longitude	Location
DHO	23.4 kHz	53.0789°N	7.615°E	Rhauderfehn, Germany
FTA	20.9 kHz	48.544632°N	2.579429°E	Sainte-Assise, France
GBZ	19.58 kHz	54.911643°N	3.278456°W	Anthorn, UK
GQD	22.1 kHz	54.9116667°N	3.2786111°W	Anthorn, UK
HWU	21.75 kHz	46.713129°N	1.245248°E	Rosnay, France
ICV	20.27 kHz	40.923127°N	9.731011°E	Isola di Tavolara, Italy
ITS	45.9 kHz	37.1°N	14.1°E	Sicilia, Italy
NAA	24.0 kHz	44.644936°N	67.281639°W	Cutler, Maine, USA
NAU	40.8 kHz	18.398762°N	67.177599°W	Aguada, Puerto Rico
NLK	24.8 kHz	48.203487°N	121.916827°W	Jim Creek, Washington, USA
NML	25.2 kHz	46.36599°N	98.335638°W	LaMoure, North Dakota, USA
NPM	21.4 kHz	21.420166°N	158.15114°W	Lualualei, Hawaii, USA
NRK	37.5 kHz	63.850365°N	22.466773°W	Grindavik, Iceland
NWC	19.8 kHz	21.816328°S	114.165586°E	North West Cape, Australia
SHF		53.382149°N	1.478302°W	Sheffield, UK
TBB	26.7 kHz	37.412725°N	27.323342°E	Bafa, Turkey

Note. Name in bold (SHF) is the receiver.

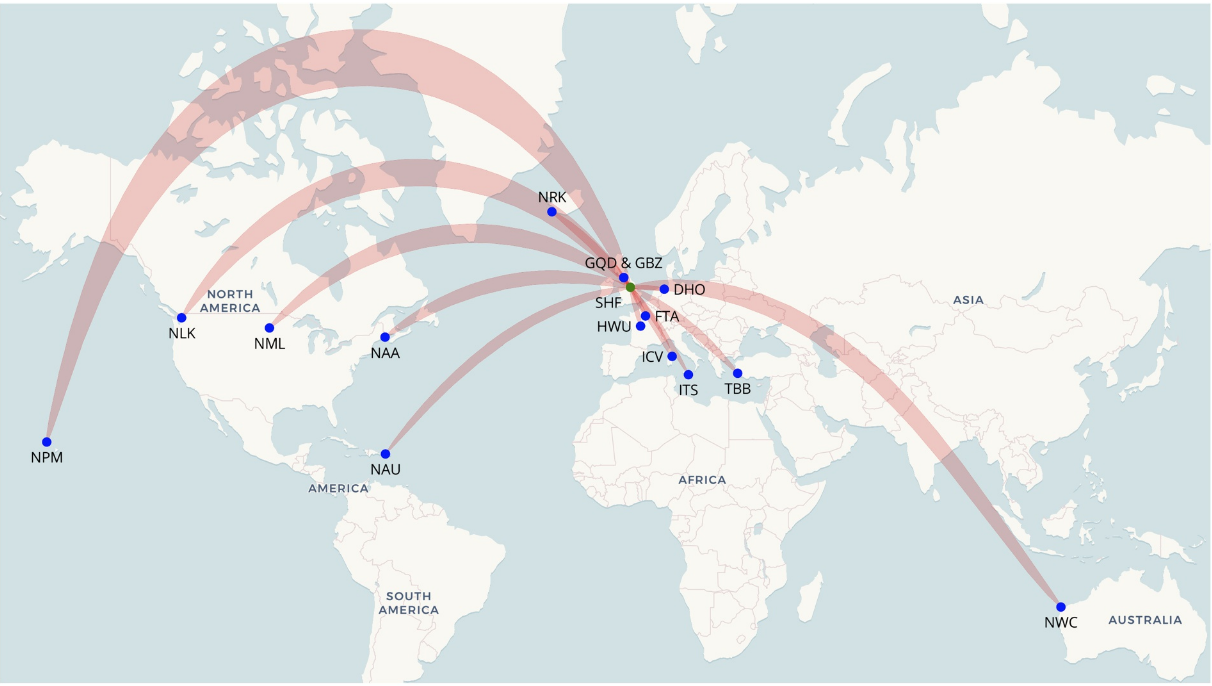

Figure 2. Geographical locations of transmitters and the receiver. The transmitters are marked in blue and the receiver in green. The first Fresnel zones of the VLF signals are shown in red.

and each signal has an amplitude and a phase, a total of 34 channels of data is analyzed. Information velocity (Γ) is used to quantify changes in the probability distribution of values measured in each of these channels. It is expected that anomalies in the signal change the signal probability distribution, which results in a higher Γ.

We use a sliding window method to temporally localize Γ. We look at small intervals of the time-series data and compare it to data from different but nearby interval. Significant differences in the distribution of values in the data from these adjacent intervals would indicate the presence of a sudden change or anomaly. Consider an interval (window) $[t, t + \tau_w]$, where τ_w is known as the window length. We choose a nearby interval by sliding this window by a value τ_s, to get $[t + \tau_s, t + \tau_w + \tau_s]$. Here τ_s is called the sliding length. We define a function $\mathcal{F}$ whose input is the interval and the output is the sequence of data from that interval:

$$\mathcal{F}([t, t + \tau_w]) = (M_t,\ M_{t+\tau_m},\ M_{t+2\tau_m}, \ldots, M_{t+\tau_w}). \tag{6}$$

Here M_t is the measurement at time t and τ_m is the measurement interval. $\tau_m = 20$ s for the data considered here. Note that $\tau_w \geq \tau_s \geq \tau_m$, and both τ_w and τ_s must be integer multiples of τ_m.

Comparison of probability distribution of signal values from two different intervals ($\mathcal{F}([t, t + \tau_w])$ and $\mathcal{F}([t + \tau_s, t + \tau_w + \tau_s])$) is made by computing the information velocity Γ given by Equation 5. Note that information velocity is interpreted as the rate of change of statistically distinguishable states.

We define $p(x, t; \tau_w)$ as the PDF of the signal values $\mathcal{F}([t, t + \tau_w])$, an example of which is shown in Figure 3. We can then compute the approximate information velocity between $p(x, t; \tau_w)$ and $p(x, t - \tau_s; \tau_w)$ by approximating the derivative and integral in Equation 7 (see Appendix A for details and the derivation):

$$\Gamma(t; \tau_s, \tau_w) = 2\sqrt{\int dx \left[\frac{\sqrt{p(x, t; \tau_w)} - \sqrt{p(x, t - \tau_s; \tau_w)}}{\tau_s}\right]^2}. \tag{7}$$

By choosing different τ_w and τ_s, we can focus on phenomena with different time scales. For instance, Figure 4 shows that there are periodic changes in VLF signals with a periodicity of 24 hr and less, likely caused by day-

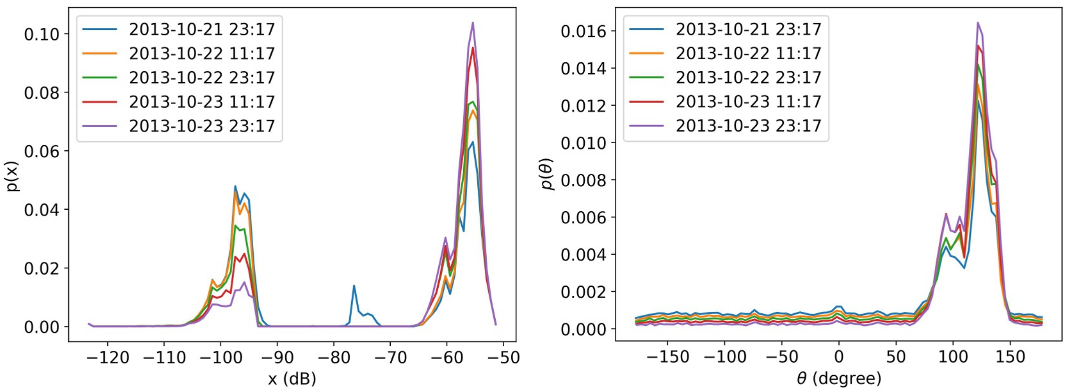

Figure 3. $p(x, t; \tau_w)$ of the amplitude (left) and phase (right) of the signal emitted by GBZ transmitter for different times t. $\tau_w = 120$ hours. The PDFs are similar except for an anomaly in the PDF of amplitude for t = 2013-10-21 23:17 (blue curve on the left).

night changes. By choosing $\tau_w < 24$ hours and calculating Γ we can capture these day-night changes. However, in this study, we select a time window τ_w exceeding 24 hr specifically to filter out day-night variations from being flagged as anomalies. With $\tau_w > 24$ hours, p (x, t; τ_w) contains the distribution of values at least throughout the 24 hr period and therefore Γ cannot capture day-night changes. Beyond this, our method identifies any event "significant" enough to alter the Probability Density Function (PDF) of the signal, either by shifting the distribution's shape (long-duration events) or extending its tails (high-intensity transients). Considering these factors and the trade-off that larger τ_w reduces noise but also reduces the impact of short-timescale anomalies, we use a somewhat arbitrary choice of $\tau_w = 5$ days and $\tau_s = 6$ hours in this study. τ_s dictates the timescale of anomalies that we are interested in. A smaller τ_s leads to better temporal resolution of anomalies, but if τ_s is too small there will be no appreciable anomalies in the signal. A thorough sensitivity analysis of these parameters would require a detailed classification of anomalies, which is beyond the scope of this study. However, a preliminary sensitivity analysis presented in Appendix B indicates the method's relative insensitivity to parameter choice.

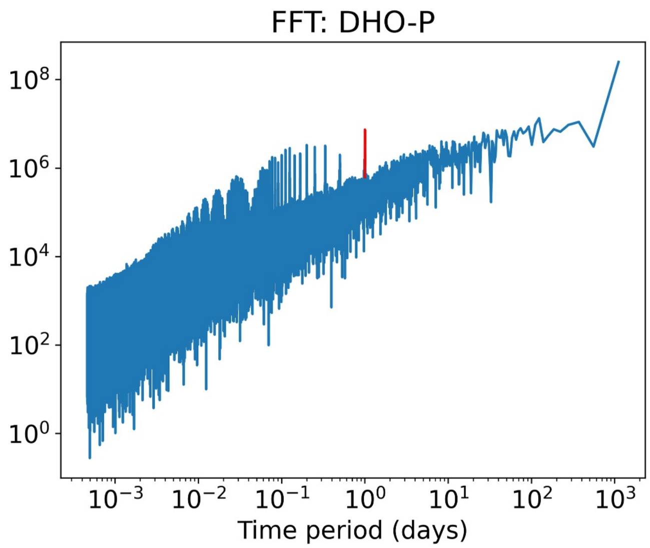

Figure 4. Absolute value of the discrete Fourier transform of phase of the DHO signal data. The data covers the time range from 2013 to 10–11 11:17:20 to 2016-10-27 16:49:00. Note that the x-axis is the inverse of the frequency. The distinguishable spikes in the plot indicate significant periodicity. The red spike indicates the periodicity with the longest duration of 1 day.

2.3. Anomaly Correlation

Let us denote the information velocity of the ith channel as $\Gamma_i(t; \tau_s, \tau_w)$. To calculate the correlation coefficient we first choose a time range τ_c and compute the Pearson correlation coefficient (ρ) between Γ_i and Γ_j in the time interval $[t - \tau_c, t]$:

$$\rho_{ij}(t; \tau_s, \tau_w, \tau_c) = \frac{\sum_{t' \in [t-\tau_c, t]} \left(\Gamma_i(t') - \bar{\Gamma}_i\right)\left(\Gamma_j(t') - \bar{\Gamma}_j\right)}{\sqrt{\sum_{t' \in [t-\tau_c, t]} \left(\Gamma_i(t') - \bar{\Gamma}_i\right)^2} \sqrt{\sum_{t' \in [t-\tau_c, t]} \left(\Gamma_j(t') - \bar{\Gamma}_j\right)^2}}. \quad (8)$$

Here the dependence of Γ on τ_s and τ_w has been omitted for brevity and $\bar{\Gamma}$ is the average of Γ over the range $[t - \tau_c, t]$.

Various atmospheric and geophysical phenomena can cause anomalies in VLF/LF signals. In addition, data corruption and numerical noise can also produce anomalies in the signal. This can be seen in Figure 5 where missing data produces the most dominant spikes in $\Gamma(t; \tau_s, \tau_w)$. Although data corruption can be fixed by following better data collection protocols and is beyond the scope of this work, there are various filtering techniques that can be used to reduce noise. Figure 6 shows the plots corresponding to Figure 5 after applying a Gaussian smoothing filter with a standard deviation of 24 hr. While there is a significant reduction in noise, it is still difficult to identify specific spikes in Γ corresponding to real-world phenomena. In order to

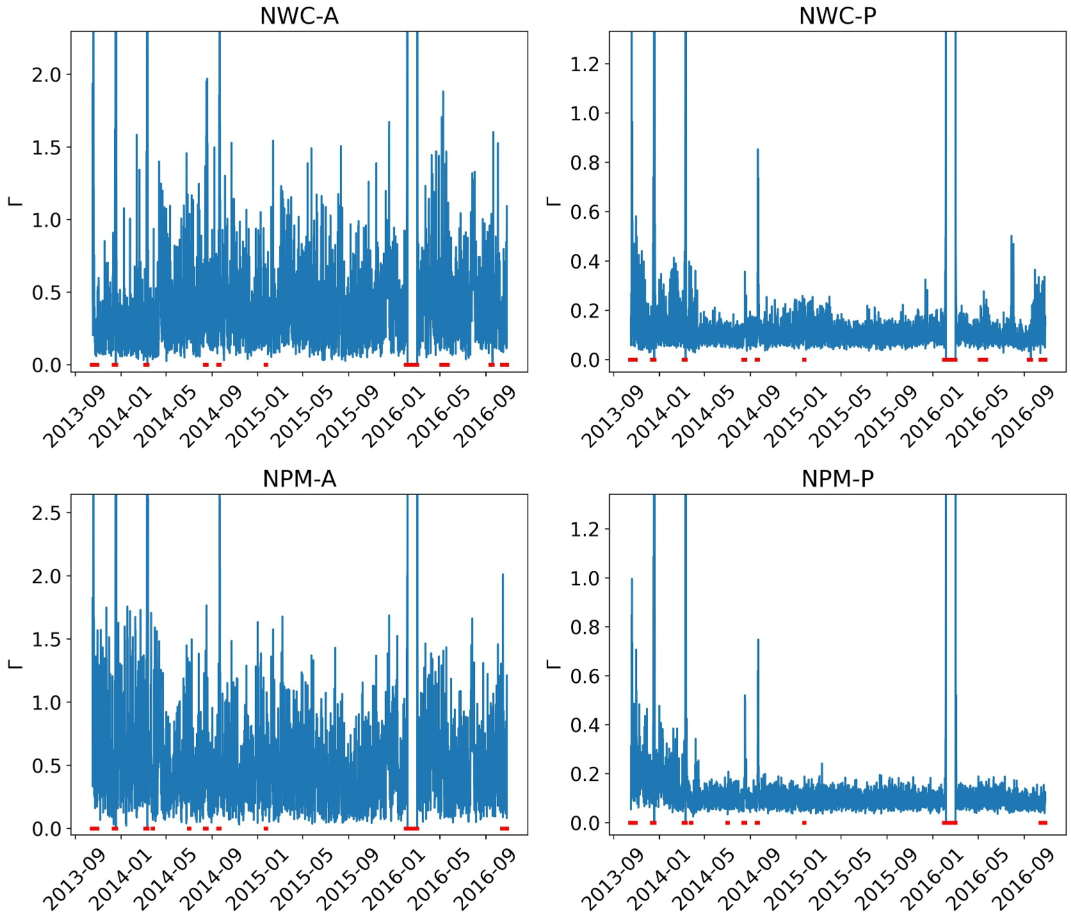

Figure 5. $\Gamma(t;\tau_s,\tau_w)$ of amplitude (denoted by 'A' in the title) and phase (denoted by 'P' in the title) of signals from NWC and NPM. Here $\tau_s = 6$ hours and $\tau_w = 120$ hours. The red markings at the bottom of the plot indicate missing values in the original time series signal.

further refine this technique, we look at the correlations of Γ from different channels. Considering anomaly correlations in such a manner helps reduce the impact of random noise as well as localize events to regions which overlap with the fresnel zones of anomaly correlated signals.

Figure 7 shows an example of an anomaly correlation for a range of days that was uneventful. The left side of the figure shows the map of pairwise anomaly correlations between all channels. The right side of the figure shows $\Gamma_i(t;\tau_s,\tau_w)$ for all the channels for the time interval $[t-\tau_c,t]$. The "A" in the title denotes the amplitude and "P" denotes the phase of the signal. $\tau_w = 5$ days and $\tau_s = 6$ hours. Note that the self-correlation given by the diagonal of the correlation map is set to zero for clarity.

3. Observations and Results

An extreme case of anomaly correlation is when emitters or receivers malfunction, resulting in corrupt or missing data. The data set used in this study contains several such artifacts. An example is provided in Figure 5. Expectedly, when such an issue is present in multiple channels simultaneously, this results in strong anomaly correlations. An example is shown in Figure 8.

A geomagnetic storm (GMS) is an example of a global atmospheric phenomenon that can produce disturbances in the ionosphere and in turn affect the VLF/LF signal propagation. In order to identify GMS events we refer to the Disturbance Storm Time (DST) index published online by the World Data Center for Geomagnetism, Kyoto (World Data Center for Geomagnetism, Kyoto, 2024). Figure 9 shows the DST index for 3 major solar activity events that occurred in 2015. These same events can be identified from the anomaly correlation map. Figure 10

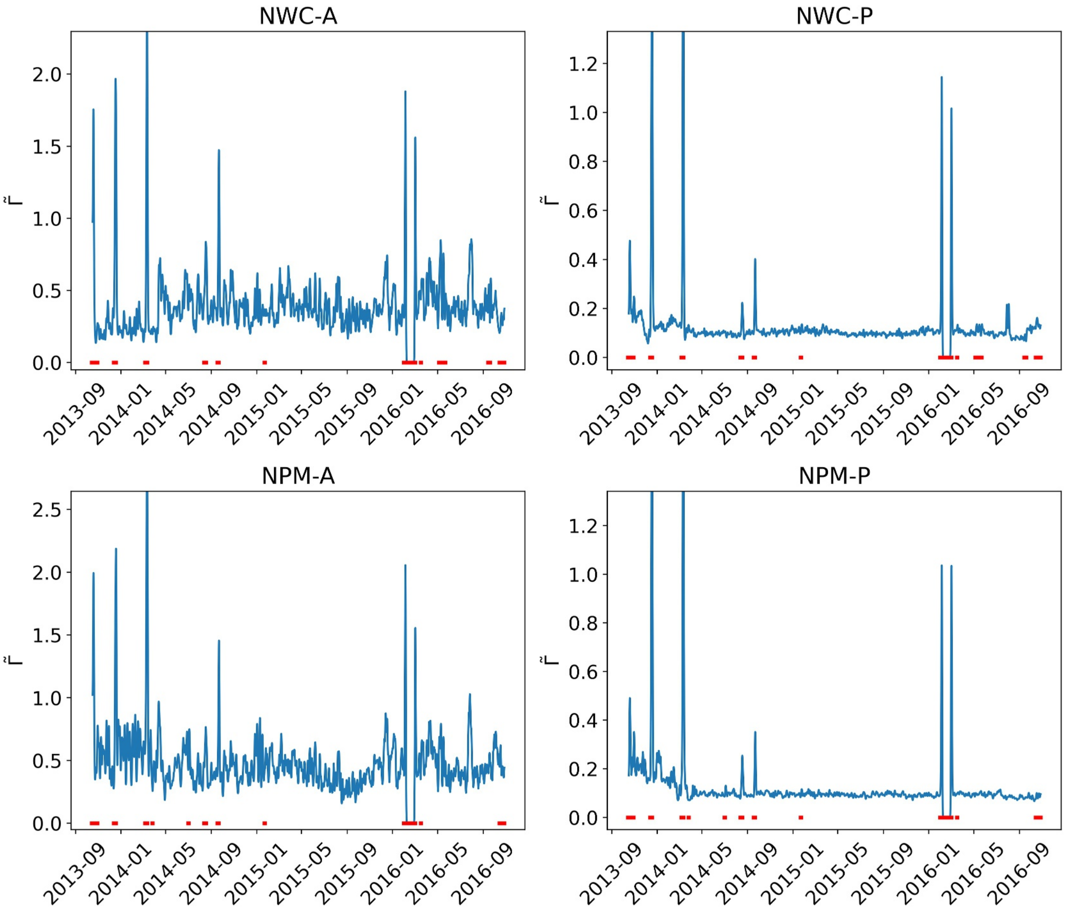

Figure 6. $\widetilde{\Gamma}(t; \tau_s, \tau_w)$ obtained after applying Gaussian smoothing with a standard deviation of 24 hr on Figure 5. Here $\tau_s = 6$ hours and $\tau_w = 120$ hours. The red markings at the bottom of the plot indicate missing values in the original time series signal.

shows anomaly correlation produced by a strong GMS event that occurred around 2015-03-18. Note that stronger anomalies are observed in signals, obtained from receiver-transmitter pairs, whose Fresnel zones are closer to the Earth's poles. This is to be expected due to the specific configuration of the Earth's magnetic fields, which deflect the solar wind particles toward the poles. Similarly the anomaly correlations for the GMS event that happened around 2015-06-23 and 2015-08-14 are shown in Figure 11.

Storms and cyclones are also known to produce disturbances in VLF signals (NaitAmor et al., 2018; Pal et al., 2020; Das et al., 2021; S. Kumar et al., 2017). Figure 12 shows the effect of Hurricane Matthew on anomaly correlation. Hurricane Matthew was a category 5 hurricane that formed around 28-09-2016 in the Atlantic and dissipated around 10-10-2016. Hurricane Matthew is expected to be the cause of the anomaly correlation between NAA-A and NAU-A channels which correspond to locations Cutler, Maine, USA and Aguada, Puerto Rico. The other anomaly correlations are between NWC-A and GBZ-A, whose emitters are located in the North West Cape, Australia and Anthorn, Cumbria, UK respectively and is likely to have been affected by some local weather phenomenon around UK. Similarly, the correlation between NLK-A, NML-A, NPM-A and TBB-A is also thought to be unrelated to Hurricane Matthew.

Figure 13 shows the effect of Cyclone Niklas on anomaly correlations. Niklas originated from a low-pressure system that formed in the North Atlantic around 2015-03-29. It then intensified and crossed the UK, reaching Western Europe on 2015-03-31. A few days before Niklas, Germany was affected by another low-pressure system, Storm Mike, around the 28th and 29th. Both plots in Figure 13 shows anomaly correlations between NLK-A, NML-A and NPM-A channels, whose fresnel zones pass over the north Atlantic, indicating the effect of Cyclone Niklas. The correlation seen in signals emitted from Germany, DHO-A and DHO-P in Figure 13 (left) is

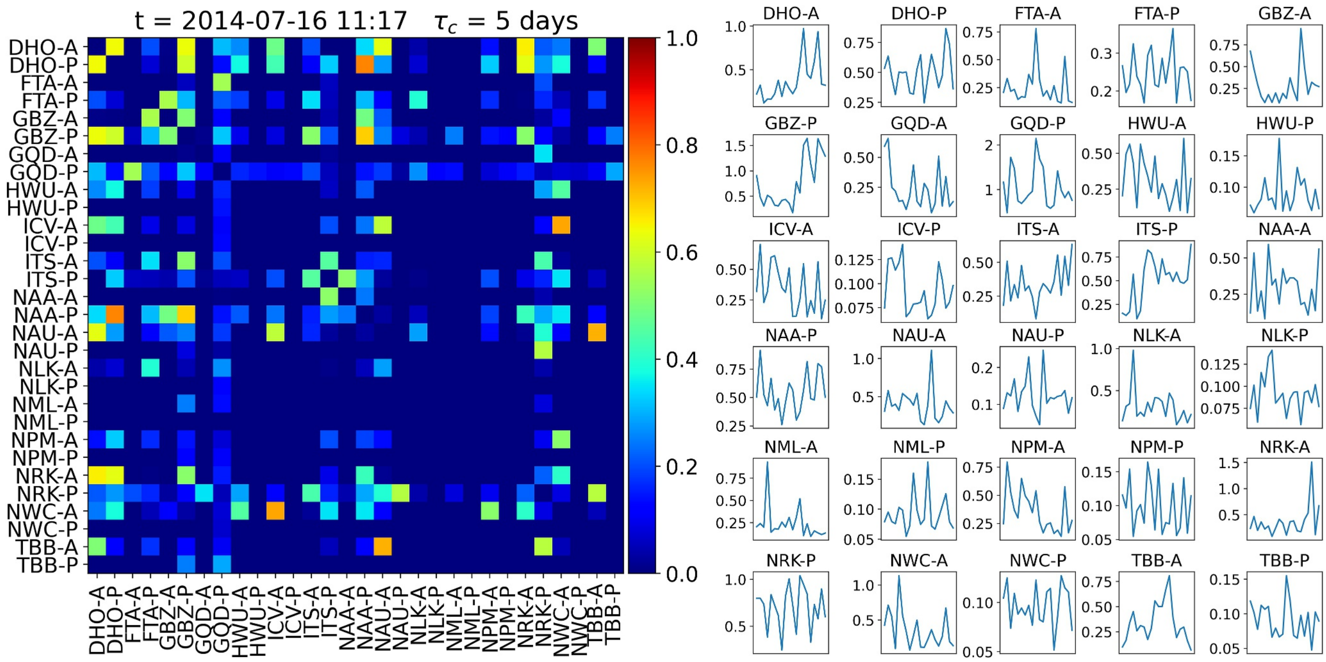

Figure 7. An example of anomaly correlation between Γ of different channels. The time frame 2014-07-11 to 2014-07-16 doesn't overlap with any notable events.

due to Storm Mike. The correlation of DHO-A and DHO-P with NRK-P located in Iceland is also indicative of the turbulent weather phenomena in this region. Figure 13 (right) shows correlations after about 18 hr, when Cyclone Niklas storm front has reached the UK and Europe. Here we can see stronger anomaly correlations among various UK and European channels. In particular we can see correlations among GBZ-A, GBZ-P and GQD-A channels located in the UK, as well as correlations between GBZ-A and NRK-A (Iceland), NWC-A (Australia) and, TBB-A (Turkey). The correlation between the Australian NWC-A channel is due to the fact that its fresnel zone passes over Europe. Besides this, anomaly correlations can be found between other channels like GBZ-A and DHO-A, NRK-P and DHO-P, TBB-A and NWC-A, NRK-A and NWC-A, indicating disturbances in Europe. The anomaly correlation in this case allows us to observe the spatial and temporal distribution of atmospheric events.

Strong anomaly correlations were primarily observed in amplitude channels across Figures 9–12, likely resulting from the higher noise levels typical of phase channels. A notable exception appears in Figure 12, where significant correlations emerge in the phase channels of DHO, NRK, GBZ, and GQD. This is corroborated by the raw data in

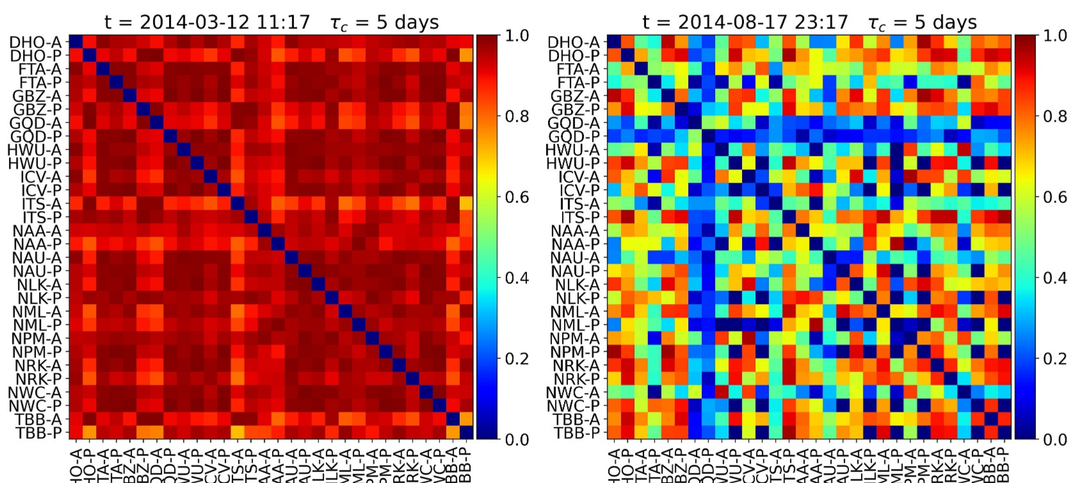

Figure 8. (Left)Missing data from all emitters (right) Partial data loss.

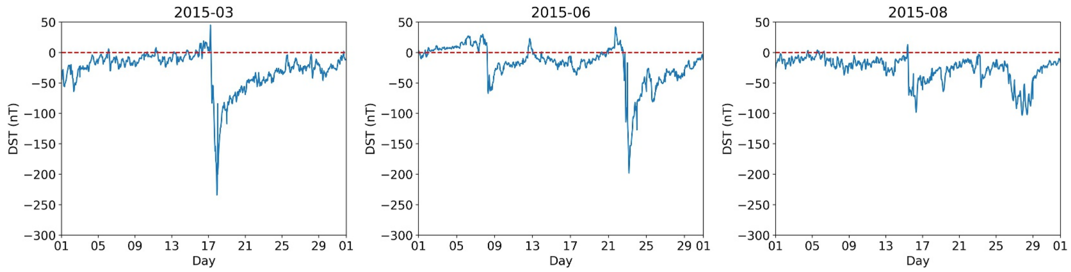

Figure 9. Disturbance Storm Time (DST) index showing the intensity of solar storms for the months 2015-03, 2015-06 and 2015-08. 0 nT is the baseline without any solar activity marked with red dashed line in the plot.

Figure 14, which shows that compared to the amplitude channels, most phase channels are noise-dominated with discernible phase signals persisting only for DHO, GQD, GBZ, ICV, ITS, NAA, and NRK. The ICV variation is unusually clean compared to other signals, and the reason is unknown. In particular, distinct diurnal variations in phase remain visible only for DHO, GQD, GBZ, and NRK, even though intermittent noise partially obscures these patterns in GQD and GBZ. Potential sources of this phase instability include reference oscillator drift, rapid fluctuations in the ionospheric reflection height, or local electromagnetic interference. While the precise origin of this noise remains indeterminate in our data set, the exact cause is immaterial to our analysis. Crucially, the model-free method developed here demonstrates sufficient robustness to automatically account for these noisy channel characteristics and identify significant anomalies regardless of the background noise source.

4. Discussion and Conclusions

In this study, we explored the application of information geometry to VLF/LF signals for anomaly detection and successfully associated these anomalies with solar storms and hurricanes. Specifically, we have demonstrated the utility of a model-free approach — information velocity (Γ) — in identifying anomalies within the amplitude and phase data of VLF signals. By analyzing anomaly correlations across multiple channels, this methodology enabled the identification of global atmospheric disturbances, including geomagnetic storms, hurricanes, and cyclones.

Our findings reveal that anomalies in VLF signals are closely linked to changes in the Earth-ionosphere waveguide, driven by atmospheric and geophysical factors. For example, geomagnetic storms, such as the event on 2015-03-18, induced significant anomalies, particularly within Fresnel zones near the poles. This behavior aligns with known geomagnetic field dynamics, where solar wind particles are funneled toward Earth's polar regions.

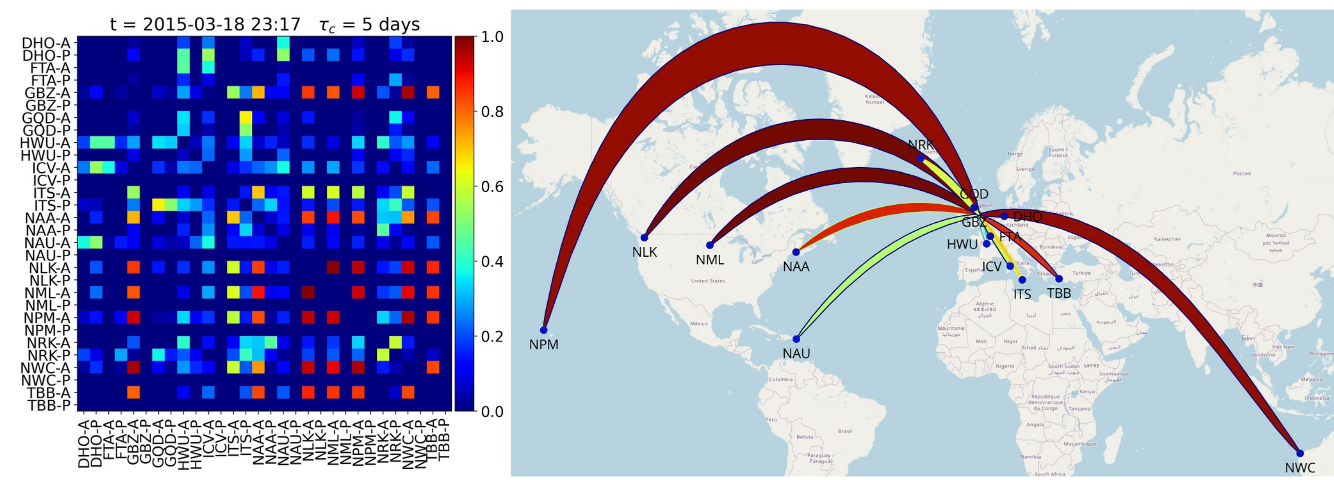

Figure 10. (left) Anomaly correlation plot corresponding to GMS which occurred around 2015-03-18 (right) Anomaly correlation visualized on a map showing the Fresnel zones. The color of each Fresnel zone denotes the value of its highest anomaly correlation with any other Fresnel zone.

10.1029/2025EA004610

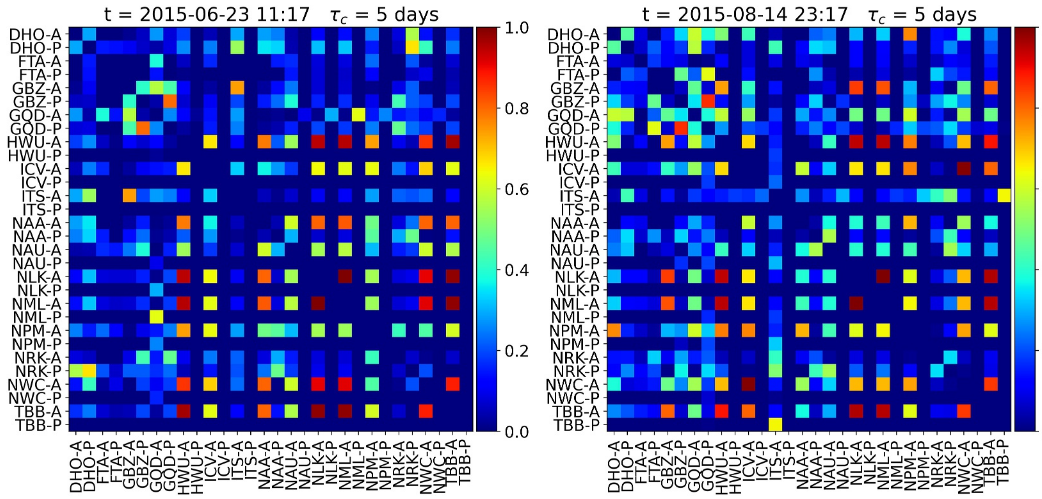

Figure 11. Anomaly correlation plot for GMS events which occurred around (left) 2015-06-23 and (right) 2015-08-14.

Similarly, weather phenomena like Hurricane Matthew and Cyclone Niklas disrupted signal propagation, as evidenced by strong anomaly correlations across specific channels.

The sliding window methodology, combined with the calculation of information velocity (Γ), proved to be highly effective for anomaly detection. Moreover, the multi-channel anomaly correlation analysis allowed us to differentiate large-scale disturbances from artifacts such as missing data or localized noise. This ensures that detected anomalies are more likely to reflect significant geophysical events rather than spurious variations.

The results also emphasize the spatial and temporal dimensions of anomaly correlations, offering valuable insights into the progression of atmospheric disturbances. For instance, the evolution of Cyclone Niklas from its formation over the North Atlantic to its landfall in Europe was captured through shifting patterns of anomaly correlations across affected channels. Such observations highlight the potential of VLF signals as a tool for monitoring dynamic atmospheric processes on a global scale.

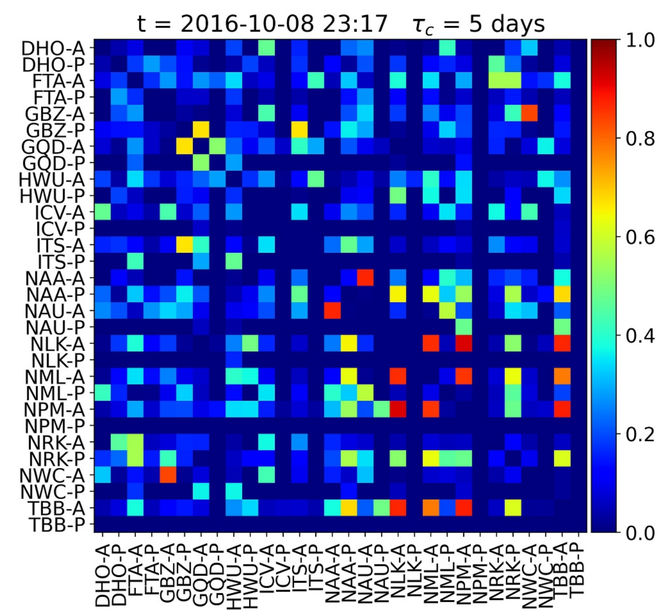

Figure 12. Anomaly correlation plot for Atlantic Hurricane Matthew.

It is of importance to clarify the limitations of the proposed method. First, as a purely statistical and model-free measure of the rate of change of the probability distribution, the information velocity (Γ) does not identify the underlying physical nature of the detected disturbances. Consequently, a physical decomposition of the signal variations or changes cannot be achieved by the method itself. While different physical phenomena might in principle introduce signature changes into the PDF, enabling decomposition into components representing distinct physical processes, identifying these signatures in practice requires either theoretical modeling of the phenomena or compiling a large labeled data set to identify these signatures using machine learning. Second, although the influence of regular diurnal variations (such as the solar terminator) is reduced by employing a window width (τ_w) greater than 24 hr to ensure that all windows capture the terminator transition, strong and irregular terminator effects can still contribute to the calculated anomalies. Third, the method itself is designed for anomaly detection and pattern correlation rather than deterministic physical attribution. Pinpointing the specific physical phenomenon causing a signal change would require combining this method with independent contextual information, such as a geomagnetic index. Finally, the thresholds for visualizing anomalies and suppressing weak correlations are chosen empirically, and establishing them formally remains an area of ongoing study.

In conclusion, this study illustrates the promise of leveraging VLF signal analysis and information geometry to investigate and predict atmospheric and

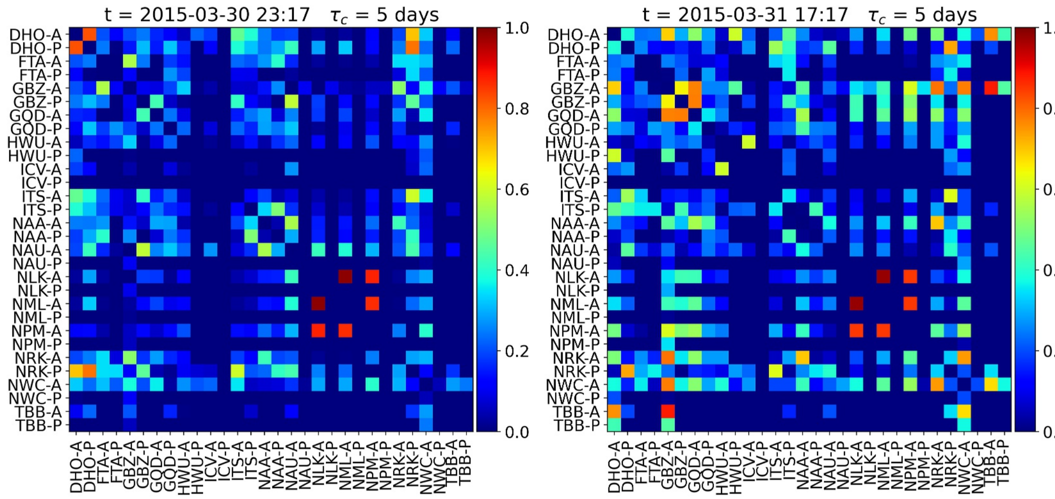

Figure 13. Anomaly correlation plot for Storm Mike and Cyclone Niklas for (left) $t = 2015\text{-}03\text{-}30$ and (right) $t = 2015\text{-}03\text{-}31$.

geophysical phenomena. Expanding the data coverage utilizing the global receiver network is crucial for enhancing localization, tracking, and predictive capabilities, while also allowing for the exploration of phenomena across varying timescales through adjustable window (τ_w) and sliding (τ_s) lengths. While our adaptive, model-free approach successfully adapts to local signal baselines and identifies statistical deviations, establishing a standardized anomaly classification criteria remains a challenge due to site-specific noise and environmental variability. To establish these thresholds more formally, future work could analyze the empirical distributions of

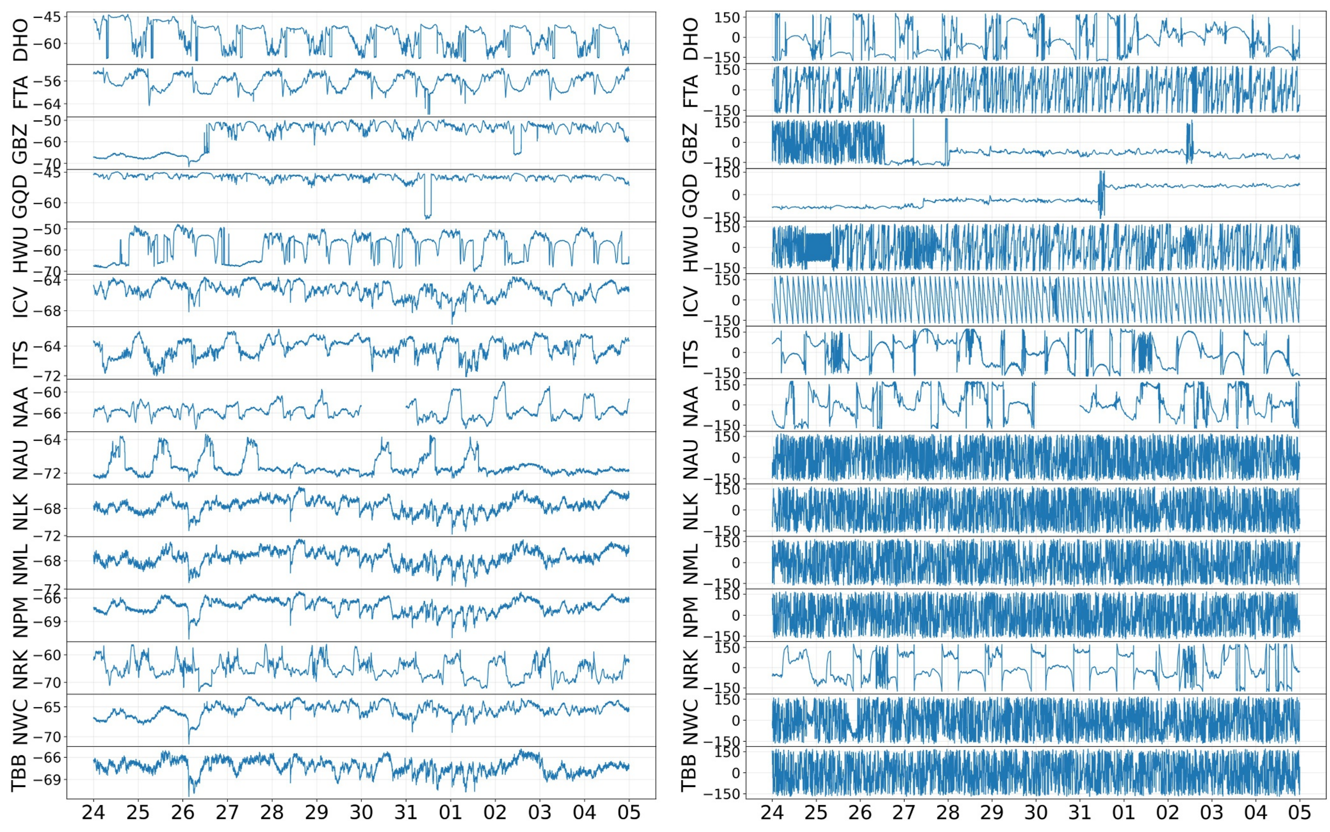

Figure 14. Plots of (left) amplitude (dB) and (right) phase (degrees) of raw data in the time range 2015-03-24 to 2015-04-05 for different receivers. A moving average smoothing was applied with 10 time points to make the plots cleaner.

information velocity during quiet periods when no events of interest are observed. A larger, multi-site corpus is also essential for the sensitivity analysis required to define these absolute thresholds, and future work must characterize natural versus artificial anomalies to filter out anthropogenic interference. Furthermore, the Fresnel zones covered in this study, did not overlap with any seismological events in the date range considered. For instance, the magnitude 5.5 earthquake (European-Mediterranean Seismological Centre, 2016) in Central Italy which occurred on 2016-10-26 at 17:10:37.1 UTC (Location: 42.880°N 13.130°E) was outside the sensitivity zones of the surrounding transmitters (ICV, ITS and TBB) and was therefore not detected. This presents an opportunity to extend this research into new domains with more diverse data sets.

Appendix A: Discretization

Time derivative can be approximated by the following finite difference expression:

$$f'(t) \approx \frac{f(t+\Delta t) - f(t)}{\Delta t}. \tag{A1}$$

Other methods of numerical differentiation exist, however are not suitable for the algorithms in this work. The error in using finite difference to approximate a derivative can be derived using the Taylor expansion:

$$f(t+\Delta t) = f(t) + f'(t)\Delta t + \frac{f''(t)\Delta t^2}{2} + \mathcal{O}(\Delta t^3) \tag{A2}$$

$$\Rightarrow f'(t) = \frac{f(t+\Delta t) - f(t)}{\Delta t} - \frac{f''(t)\Delta t}{2} + \mathcal{O}(\Delta t^2). \tag{A3}$$

An integral can be approximated using the trapezoidal rule:

$$\int_a^b f(t)dt \approx \sum_{k=1}^{N} \frac{f(t_{k-1}) + f(t_k)}{2} \Delta t_k, \tag{A4}$$

where the interval (a, b) is divided into N sub-intervals and $\Delta t_k := t_k - t_{k-1}$. If the sub-intervals have equal width, the error in the approximation is bounded (Cruz-Uribe & Neugebauer, 2003):

$$\left| \int_a^b f(t)dt - \sum_{k=1}^{N} \frac{f(t_{k-1}) + f(t_k)}{2} \Delta t_k \right| \le \max_{a \le t \le b} |f''(t)| \frac{(b-a)^3}{12N^2}. \tag{A5}$$

Appendix B: Preliminary Sensitivity Analysis Results

Figure B1 presents the sensitivity analysis for τ_w and τ_s. From the left panel, we observe that increasing τ_w leads to a decrease in the magnitude of information velocity values. This is because a larger τ_w increases the number of samples used in the PDF estimation, thereby reducing the statistical noise relative to the fixed τ_s. Despite this change in magnitude, the overall patterns in the signal remain largely consistent with minor details being drowned out when increasing τ_w. In the right panel, adjusting τ_s results in minimal differences, with the patterns remaining stable. Decreasing τ_s yields slightly larger values, as the same amount of probability distribution change is observed over a shorter time span, effectively increasing the information velocity. This behavior is specific to the characteristics of the data set considered. Overall, the major patterns in the plots remain identifiable, indicating a relative insensitivity to the choice of τ_w and τ_s. However, the sensitivity analysis for τ_c is omitted as its behavior is trivial: since τ_c defines the time period for correlation calculation, the resulting correlations are directly and predictably determined by the temporal persistence of the anomalies, and are subject to the type of events and data sets considered.

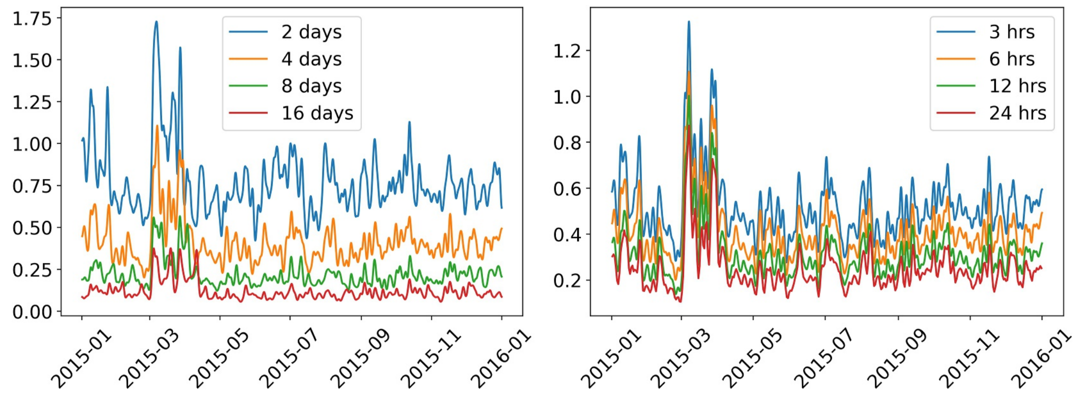

Figure B1. $\widetilde{\Gamma}(t; \tau_s, \tau_w)$ obtained after applying Gaussian smoothing with a standard deviation of 24 hr to information velocity (Γ) of amplitude channel of GBZ for (left) constant $\tau_s = 6$ hrs and varying τ_w and (right) constant $\tau_w = 4$ days and varying τ_s. The Gaussian smoothing is applied to reduce noise. The choice of date range from 2015 to 01-01 to 2016-01-01 was made so that no data collection gaps occurred during this period.

Conflict of Interest

The authors declare no conflicts of interest relevant to this study.

Availability Statement

The data supporting the conclusions of this study are openly available at the Flinders University Research Data Repository (Thiruthummal et al., 2026).

Acknowledgments
We would like to acknowledge the support and resources provided by the Centre for Fluid and Complex Systems at Coventry University, UK; the School of Information Technology at Deakin University, Australia; the College of Science and Engineering at Flinders University, Australia; and the Plasma Dynamics Group in the School of Electrical and Electronic Engineering at the University of Sheffield, UK. We are grateful to the designers of the UltraMSK software-defined radio system for the receiver located in Sheffield, UK, which made the collection of VLF/LF signal amplitude and phase data possible. We also thank the World Data Center for Geomagnetism, Kyoto, for providing the Disturbance Storm Time (DST) index data.

References

Bezděková, B., Němec, F., & Manninen, J. (2022). Ground-based VLF wave intensity variations investigated by the principal component analysis. *Earth Planets and Space*, *74*(1), 30. https://doi.org/10.1186/s40623-022-01588-4

Chang, D., & Helliwell, R. (1980). VLF pulse propagation in the magnetosphere. *IEEE Transactions on Antennas and Propagation*, *28*(2), 170–176. https://doi.org/10.1109/tap.1980.1142297

Chernogor, L. (2010). Variations in the amplitude and phase of VLF radiowaves in the ionosphere during the August 1, 2008, solar eclipse. *Geomagnetism and Aeronomy*, *50*(1), 96–106. https://doi.org/10.1134/s0016793210010111

Clilverd, M. A., Rodger, C. J., Thomson, N. R., Lichtenberger, J., Steinbach, P., Cannon, P., & Angling, M. J. (2001). Total solar eclipse effects on VLF signals: Observations and Modeling. *Radio Science*, *36*(4), 773–788. https://doi.org/10.1029/2000rs002395

Cruz-Uribe, D., & Neugebauer, C. (2003). An elementary proof of error estimates for the trapezoidal rule. *Mathematics Magazine*, *76*(4), 303–306. https://doi.org/10.1080/0025570x.2003.11953199

Das, B., Sarkar, S., Haldar, P. K., Midya, S. K., & Pal, S. (2021). D-region ionospheric disturbances associated with the extremely severe cyclone Fani over North Indian Ocean as observed from two tropical VLF stations. *Advances in Space Research*, *67*(1), 75–86. https://doi.org/10.1016/j.asr.2020.09.018

Diosi, L., Kulacsy, K., Lukacs, B., & Racz, A. (1996). Thermodynamic length, time, speed, and optimum path to minimize entropy production. *The Journal of chemical physics*, *105*(24), 11220–11225. https://doi.org/10.1063/1.472897

Eftaxias, K., Kapiris, P., Polygiannakis, J., Peratzakis, A., Kopanas, J., Antonopoulos, G., & Rigas, D. (2003). Experience of short term earthquake precursors with VLF–VHF electromagnetic emissions. *Natural Hazards and Earth System Sciences*, *3*(3/4), 217–228. https://doi.org/10.5194/nhess-3-217-2003

European-Mediterranean Seismological Centre. (2016). Earthquake information: Magnitude 5.5, central Italy. Retrieved from https://www.emsc-csem.org/Earthquake_information/earthquake.php?id=539614

Frieden, B. R. (2004). *Science from Fisher information: A Unification* (2nd ed.). Cambridge University Press. https://doi.org/10.1017/CBO9780511616907

Gangbo, W., & McCann, R. J. (1996). The geometry of optimal transportation. *Acta Mathematica*, *177*(2), 113–161. https://doi.org/10.1007/bf02392620

Gibbs, A. L., & Su, F. E. (2002). On choosing and bounding probability metrics. *International Statistical Review*, *70*(3), 419–435. https://doi.org/10.1111/j.1751-5823.2002.tb00178.x

Gross, N., & Cohen, M. (2020). VLF remote sensing of the D region ionosphere using neural networks. *Journal of Geophysical Research: Space Physics*, *125*(1), e2019JA027135. https://doi.org/10.1029/2019ja027135

Guel-Cortez, A.-J., & Kim, E.-j. (2021). Information geometric theory in the prediction of abrupt changes in system dynamics. *Entropy*, *23*(6), 694. https://doi.org/10.3390/e23060694

Güzel, E., Canyilmaz, M., & Türk, M. (2011). Application of wavelet-based denoising techniques to remote sensing very low frequency signals. *Radio Science*, *46*(2), 1–9. https://doi.org/10.1029/2010rs004449

Hayakawa, M. (1996). The precursory signature effect of the Kobe earthquake on VLF subionospheric signals. *Journal of the Communications Research Laboratory*, *43*, 169–180.

Hayakawa, M., Kasahara, Y., Nakamura, T., Muto, F., Horie, T., Maekawa, S., et al. (2010). A statistical study on the correlation between lower ionospheric perturbations as seen by subionospheric VLF/LF propagation and earthquakes. *Journal of Geophysical Research*, *115*(A9). https://doi.org/10.1029/2009ja015143

Hayakawa, M., Molchanov, O., & NASDA/UEC team. (2004). Summary report of NASDA's earthquake remote sensing frontier project. *Physics and Chemistry of the Earth, Parts A/B/C*, *29*(4–9), 617–625. https://doi.org/10.1016/j.pce.2003.08.062

Hayakawa, M., Molchanov, O. A., Ondoh, T., & Kawai, E. (1996). Anomalies in the sub-ionospheric VLF signals for the 1995 Hyogo-Ken Nanbu earthquake. *Journal of Physics of the Earth*, *44*(4), 413–418. https://doi.org/10.4294/jpe1952.44.413

Inan, U. S., Cummer, S. A., & Marshall, R. A. (2010). A survey of ELF and VLF research on lightning-ionosphere interactions and causative discharges. *Journal of Geophysical Research*, *115*(A6). https://doi.org/10.1029/2009ja014775

Jones, D. (1973). Pattern recognition for VLF studies. *Radio Science*, *8*(5), 467–473. https://doi.org/10.1029/rs008i005p00467

Kim, E.-j. (2021). Information geometry, fluctuations, non-equilibrium thermodynamics, and geodesics in complex systems. *Entropy*, *23*(11), 1393. https://doi.org/10.3390/e23111393

Kim, E.-j., & Guel-Cortez, A.-J. (2021). Causal information rate. *Entropy*, *23*(8), 1087. https://doi.org/10.3390/e23081087

Kumar, A., & Kumar, S. (2018). Solar flare effects on D-region ionosphere using VLF measurements during low-and high-solar activity phases of Solar Cycle 24. *Earth Planets and Space*, *70*(1), 1–14. https://doi.org/10.1186/s40623-018-0794-8

Kumar, S., NaitAmor, S., Chanrion, O., & Neubert, T. (2017). Perturbations to the lower ionosphere by tropical cyclone Evan in the south Pacific region. *Journal of Geophysical Research: Space Physics*, *122*(8), 8720–8732. https://doi.org/10.1002/2017ja024023

Majtey, A., Lamberti, P. W., Martin, M. T., & Plastino, A. (2005). Wootters' distance revisited: A new distinguishability criterium. *The European Physical Journal D-Atomic, Molecular, Optical and Plasma Physics*, *32*(3), 413–419. https://doi.org/10.1140/epjd/e2005-00005-1

Maurya, A. K., Phanikumar, D., Singh, R., Kumar, S., Veenadhari, B., Kwak, Y.-S., & Niranjan Kumar, K. (2014). Low-mid latitude D region ionospheric perturbations associated with 22 July 2009 total solar eclipse: Wave-like signatures inferred from VLF observations. *Journal of Geophysical Research: Space Physics*, *119*(10), 8512–8523. https://doi.org/10.1002/2013ja019521

McRae, W. M., & Thomson, N. R. (2004). Solar flare induced ionospheric D-region enhancements from VLF phase and amplitude observations. *Journal of Atmospheric and Solar-Terrestrial Physics*, *66*(1), 77–87. https://doi.org/10.1016/j.jastp.2003.09.009

Molchanov, O., & Hayakawa, M. (1998). Subionospheric VLF signal perturbations possibly related to earthquakes. *Journal of Geophysical Research*, *103*(A8), 17489–17504. https://doi.org/10.1029/98ja00999

Molchanov, O., Hayakawa, M., Oudoh, T., & Kawai, E. (1998). Precursory effects in the subionospheric VLF signals for the Kobe earthquake. *Physics of the Earth and Planetary Interiors*, *105*(3–4), 239–248. https://doi.org/10.1016/s0031-9201(97)00095-2

Molchanov, O., Rozhnoi, A., Solovieva, M., Akentieva, O., Berthelier, J.-J., Parrot, M., et al. (2006). Global diagnostics of the ionospheric perturbations related to the seismic activity using the VLF radio signals collected on the DEMETER satellite. *Natural Hazards and Earth System Sciences*, *6*(5), 745–753. https://doi.org/10.5194/nhess-6-745-2006

NaitAmor, S., Cohen, M., Kumar, S., Chanrion, O., & Neubert, T. (2018). VLF signal anomalies during cyclone activity in the Atlantic Ocean. *Geophysical Research Letters*, *45*(19), 10–185. https://doi.org/10.1029/2018gl078988

Nardi, A., Pignatelli, A., & Spagnuolo, E. (2022). A neural network based approach to classify VLF signals as rock rupture precursors. *Scientific Reports*, *12*(1), 13744. https://doi.org/10.1038/s41598-022-17803-x

Pal, S., Sarkar, S., Midya, S. K., Mondal, S. K., & Hobara, Y. (2020). Low-latitude VLF radio signal disturbances due to the extremely severe cyclone Fani of May 2019 and associated mesospheric response. *Journal of Geophysical Research: Space Physics*, *125*(5), e2019JA027288. https://doi.org/10.1029/2019ja027288

Raulin, J.-P., Bertoni, F. C., Gavilán, H. R., Guevara-Day, W., Rodriguez, R., Fernandez, G., et al. (2010). Solar flare detection sensitivity using the South America VLF network (SAVNET). *Journal of Geophysical Research*, *115*(A7), A07301. https://doi.org/10.1029/2009ja015154

Righetti, F., Biagi, F., Maggipinto, T., Schiavulli, L., Ligonzo, T., Ermini, A., et al. (2012). Wavelet analysis of the LF radio signals collected by the European VLF/LF network from July 2009 to April 2011. *Annals of Geophysics*, *55*(1). https://doi.org/10.4401/ag-5188

Rozhnoi, A., Solovieva, M., Levin, B., Hayakawa, M., & Fedun, V. (2014). Meteorological effects in the lower ionosphere as based on VLF/LF signal observations. *Natural Hazards and Earth System Sciences*, *14*(10), 2671–2679. https://doi.org/10.5194/nhess-14-2671-2014

Rozhnoi, A., Solovieva, M., Molchanov, O., Schwingenschuh, K., Boudjada, M., Biagi, P., et al. (2009). Anomalies in VLF radio signals prior the Abruzzo earthquake (m=6.3) on 6 April 2009. *Natural Hazards and Earth System Sciences*, *9*(5), 1727–1732. https://doi.org/10.5194/nhess-9-1727-2009

Rozhnoi, A., Solovieva, M., Parrot, M., Hayakawa, M., Biagi, P.-F., Schwingenschuh, K., & Fedun, V. (2015). VLF/LF signal studies of the ionospheric response to strong seismic activity in the far Eastern region combining the DEMETER and ground-based observations. *Physics and Chemistry of the Earth, Parts A/B/C*, *85*, 141–149. https://doi.org/10.1016/j.pce.2015.02.005

Sorokin, V., & Pokhotelov, O. (2014). Model for the VLF/LF radio signal anomalies formation associated with earthquakes. *Advances in Space Research*, *54*(12), 2532–2539. https://doi.org/10.1016/j.asr.2013.11.048

Thiruthummal, A. A., Shelyag, S., Fedun, V., Ruzheinikov, S., & Kim, E.-j. (2026). Data for: An information geometry-based method to study atmospheric and seismic phenomena with VLF signals. *Flinders University Research Data Repository*. https://doi.org/10.25451/flinders.28836746

Thomson, N. R., & Clilverd, M. A. (2000). Solar cycle changes in daytime VLF subionospheric attenuation. *Journal of Atmospheric and Solar-Terrestrial Physics*, *62*(7), 601–608. https://doi.org/10.1016/s1364-6826(00)00026-2

UltraMSK. (2026). UltraMSK: VLF MSK receiver. Retrieved from https://www.ultramsk.com/

Wang, J., Huang, Q., Ma, Q., Chang, S., He, J., Wang, H., et al. (2020). Classification of VLF/LF lightning signals using sensors and deep learning methods. *Sensors*, *20*(4), 1030. https://doi.org/10.3390/s20041030

Williams, E., & Sátori, G. (2007). Solar radiation-induced changes in ionospheric height and the Schumann resonance waveguide on different timescales. *Radio Science*, *42*(2), 1–8. https://doi.org/10.1029/2006rs003494

Wootters, W. K. (1981). Statistical distance and Hilbert space. *Physical Review D*, *23*(2), 357–362. https://doi.org/10.1103/physrevd.23.357

World Data Center for Geomagnetism, Kyoto. (2024). Dst index–World data center for geomagnetism. Retrieved from https://wdc.kugi.kyoto-u.ac.jp/dst_final/index.html